Topology Optimization of Chip Inductor Using Density Method

Shuli Yin[1], Hajime Igarashi[2], and Stéphane Clénet[3]

[1]State Key Laboratory of Electrical Insulation and Power Equipment, Xi'an Jiaotong University, China
[2]D-RED: Data-Driven Interdisciplinary Research Emergence Department, Hokkaido University, Japan
[3]Univ. Lille, Arts et Métiers Institute of Technology, Centrale Lille, Junia, ULR 2697 - L2EP, F-59000 Lille, France

This paper proposes a novel methodology of the topology optimization method considering eddy current effects. The method is applied on chip inductors modelled by the Finite Element Method (FEM). Aiming to meet a specified inductance value while minimizing eddy current losses, we employ a density-based approach to construct a continuous material distribution. The derivative of the objective function with respect to the material distribution is obtained using the adjoint variable method, then the material layout is iteratively updated via the L-BFGS-B algorithm. The proposed framework is validated on both single-turn and multi-turn inductor structures, achieving designs that satisfy the target performance within a limited number of iterations. A key innovation of this work lies in the integration of field-circuit coupling into the topology optimization framework, enabling the analysis of inductors under complex coil configurations involving both series and parallel connections. Additionally, we present an original derivation of the sensitivity formulation associated with the inductance value ensuring that the optimized inductance meets the design specification.

***Index Terms*— adjoint variable method, density-based FEM, eddy current, field-circuit coupling.**

I. Introduction

CHIP INDUCTORS are in huge demand in systems of the power electronics due to their high level of integration, typically with dimensions on the millimeter scale [1]. To enhance inductance, chip inductors are typically designed with multiple-turn spiral coil structures connected in series. Research has focused on the design and optimization of such multi-turn inductors, especially those utilizing series-connected spiral configurations [2].

However, in PCB implementations, depending on the operation frequency, solid wires with increasing widths could lead to severe skin effects. To address this issue, parallel multitrack solutions have been proposed, which split single traces into finer rectangular tracks [1], [3]-[4].

These parallel multi-track techniques, while effective in mitigating skin effects, essentially introduce parallel current paths within the multi-turn coil structure. In other words, the coil in a chip inductor often adopts a hybrid configuration combining both series and parallel connections, which significantly increases the complexity of design, modeling, and topology optimization.

Benefiting from the development of topology optimization methodologies, the application of these techniques to the design of inductors and similar electromagnetic devices has become increasingly widespread. Optimization algorithms are generally classified into gradient-based [5]-[8] and gradient-free methods [9]. Due to the advantages of gradient-based density methods, such as their computational efficiency, smooth material interpolation, and ease of sensitivity analysis, they have attracted considerable attention from researchers [5]-[8].

Among them, [5] investigates topology optimization of the ferromagnetic core in inductors, aiming to maximize the value of inductance; [6] minimizes the torque ripple of synchronous reluctance machine rotors by optimizing electrical steel. Regarding the topology optimization of the coil, [7] optimizes the geometry of the stator teeth with the objective of maximizing magnetic energy. However, most existing studies on coil topology optimization are primarily based on single-turn coil configurations. To enable topology optimization of multi-turn coils, [8] proposes the density-based method for designing the windings of coreless electrical machines. However, the approach assumes that each turn shares an identical cross-sectional topology, and the primary focus is on addressing the spatial interference among multiple windings during the optimization process. To the best of our knowledge, there is no existing topology optimization study that integrates the design of ferromagnetic materials with coil optimization, while simultaneously addressing both parallel and series circuit configurations within the coil structure.

This paper presents a novel methodology for chip inductor design via topology optimization. Different from most existing literature which focuses primarily on maximization/ minimization problems, we present an original derivation process to ensure that the inductance meets specific target value. Meanwhile, in each iteration, the proposed method analytically computes the gradients associated with both inductance and Joule loss. This dual-gradient evaluation, combined with the rapid convergence characteristics of gradient-based optimization, results in a highly efficient optimization process. It has been verified that when the inductance of the initial topology is close to the target design value, the proposed method can efficiently and rapidly achieve highly satisfactory optimization results.

Moreover, we integrate a field-circuit coupled approach into the topology optimization process to analyze design outcomes under simultaneous parallel and series coil configurations, addressing a critical gap rarely explored in existing studies.

II. Model Description and Formulations

A. Model Description

In this work, 2D inductors are determined by considering

Corresponding author: Shuli Yin (e-mail: shuli.yin@xjtu.edu.cn).

both the single-turn (Fig. 1 (a)) and the multi-turn configurations which takes the two-turn coil as a representative example (Fig. 1 (b)). Each turn occupies one distinct design domain. The design region is assumed to consist of square units with dimensions $l \times l$. Using the density-based method, the material distribution within these domains can be determined. The materials are either copper or iron. The conductivity σ and reluctivity ν of copper are 5.8×10^7 S/m and 7.96×10^5 A · m/Wb, respectively, while those of iron are 0 S/m and 7.96×10^2 A · m/Wb, preventing any current flow through the iron region.

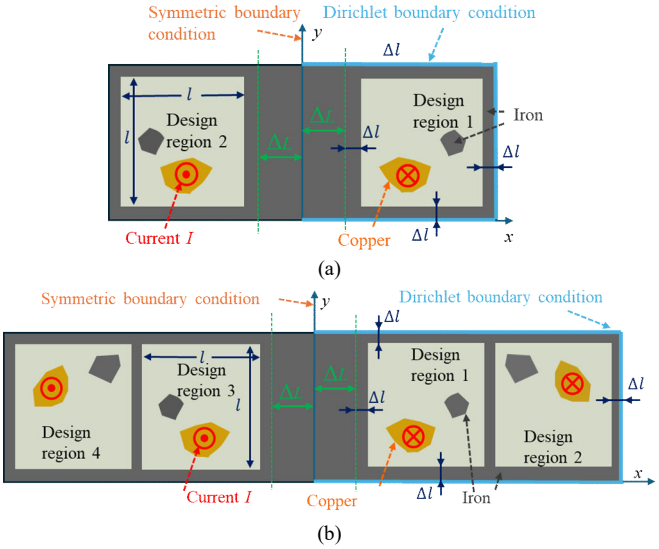

Fig. 1. Illustration of the 2D inductors to be optimized. (a) Geometric structure and boundary conditions of a single-turn case. (b) Geometric structure and boundary conditions of a two-turn case.

Additionally, each region is surrounded by an iron boundary layer with a width (denoted by Δl) of 0.1mm, and an iron core with a width ΔL is placed along the axis of symmetry.

To achieve symmetry in the topology, the structure is designed such that, upon applying excitation, the current I flows into the cross-section on the right side of the symmetric axis, and out of the cross-section on the left side. Therefore, only half of the geometry needs to be optimized. Specifically, in the case of the single-turn inductor shown in Fig. 1 (a), only *Design region* 1 needs to be optimized; whereas for the two-turn inductor in Fig. 1 (b), only *Design region* 1 and *Design region* 2 are required for optimization.

The lumped circuit models for the single-turn and multi-turn inductors are shown in Fig. 2. It can be observed that, within each design region, electrically isolated conductors are connected in parallel, while conductors between different design regions are connected in series. Here, we assume an external excitation V_{ext} of a 50 kHz voltage source with an amplitude of 2 V.

In this study, we aim to design inductors such that the resulting inductance L approaches the target value L_{tar}, while minimizing the Joule loss J_{loss}. This can be expressed using the objective function F, which is normalized and satisfies:

$$F = \alpha\left(W_1\frac{\left(L-L_{tar}\right)^2}{L_{tar}^{\ 2}}+W_2\frac{J_{loss}}{J_0}\right)\rightarrow \min.\,, \tag{1}$$

in which W_1 and W_2 are weighting coefficients, α is the scaling factor for amplifying F and its gradient, and J_0 is the reference value and equal to 1 W. Equation (1) motivates the choice of imposing of voltage V_{ext} instead of a current I. This is because, as will be explained later, the proposed topology optimization method involves materials with continuously varying conductivities. During the material variation process, certain areas may possess extremely low electrical conductivity. Imposing a constant current source would cause J_{loss} to become excessively large, and its sensitivity with respect to material distribution would become highly irregular, thereby hindering convergence in the optimization process.

It is worth emphasizing that, the purpose of formulating F in this manner is to first obtain an inductor that meets the target inductance. Then the design can be fine-tuned to reduce Joule loss. Therefore, at the beginning of the optimization, the first term of F has a dominant influence. As the search gradually stabilizes, the magnitude of the first term becomes comparable to that of the second term, resulting in a mutual constraint that promotes balanced convergence between the associated objectives.

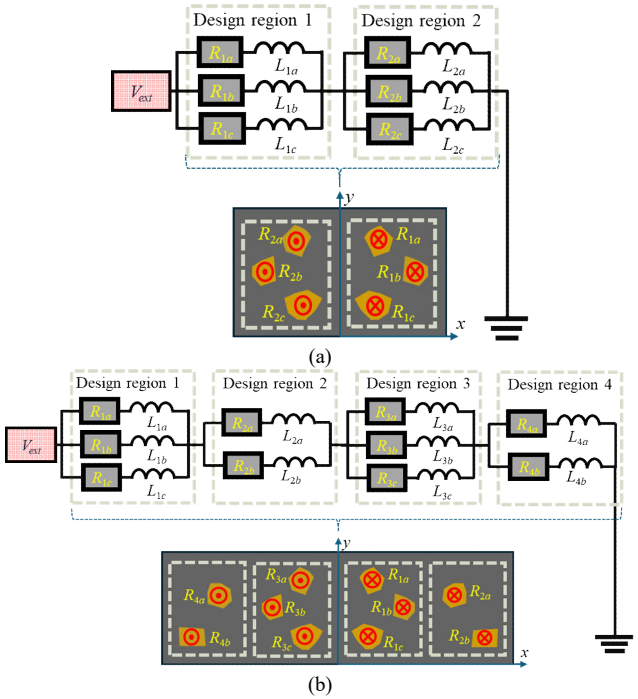

Fig. 2. Lumped circuit diagrams. (a) A single-turn case. (b) A two-turn case.

B. *Density-based FEM*

To achieve the topology optimization defined by objective function (1), the density-based method combined with the FEM is employed in this work. Specifically, to ensure the continuity and differentiability of material variations, we define the density ρ ($0\leq\rho\leq1$) in combination with the sigmoid function f

$$f(\rho)=\frac{1}{1+\exp(-\alpha\rho+\beta)} \tag{2}$$

to approximate σ or ν of materials [10]:

$$x(\rho) \approx x_{iron}\left(1-f(\rho)\right)+x_{cop}f(\rho), \tag{3}$$

where x represents the material conductivity or permeability, x_{iron} and x_{cop} represents the *conductivity* or the *permeability* of iron and copper respectively. In (2), α, β are the slope parameter equal to 10.0, and the projection center equal to 5.0 in this paper. Based on (3), the material variation illustrated in Fig. 3, from which It can be observed that the material is iron when ρ is 0 and copper when ρ is 1. In addition, due to the inherent characteristics of the sigmoid function, f approaches 0 and 1 as ρ tends to 0 and 1, respectively, but never exactly reaches these limits. To address this issue, we introduce a parameter $\Delta\rho$ (equal to be 0.01 in this work), such that when $\rho < \Delta\rho$ or $\rho > 1-\Delta\rho$, f is explicitly set to 0 and 1, respectively, as illustrated in Fig. 3.

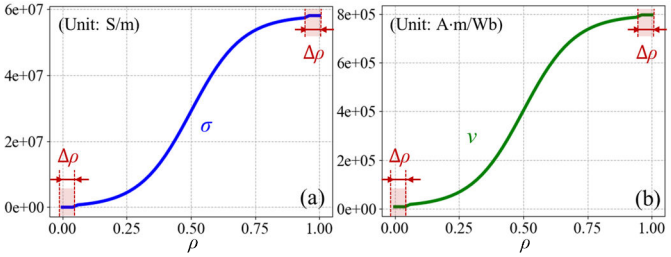

Fig. 3. Density-based electrical and magnetic properties. (a) Conductivity. (b) Reluctivity.

Following this, FEM is used to discretized the 2D magnetoquasistatic problem using the vector potential formulation. We obtain the following system of equations:

$$\mathbf{K}\boldsymbol{A} + j\omega\mathbf{M}\boldsymbol{A} = \mathbf{Q}\boldsymbol{V}/l_z\,, \tag{4}$$

where $\boldsymbol{A}$ is the vector of the values of the vector potential at the node of the mesh, $\mathbf{K}$ is the stiffness matrix, $\mathbf{M}$ is the mass matrix, and $\mathbf{Q}$ is the load matrix with corresponding expressions for the (i, j)-th elements given by:

$$k_{ij} = \int_\Omega \nu(\rho)\nabla N_i \cdot \nabla N_j d\Omega\,, \tag{5}$$

$$M_{ij} = \int_\Omega \sigma(\rho) N_i N_j d\Omega\,, \tag{6}$$

$$Q_{ij} = \int_\Omega \sigma(\rho) N_i d\Omega\,, \tag{7}$$

respectively, in which $N_{i(j)}$ is the nodal basis function [11], and Ω is the computational domain. It can be seen that both ν in $\mathbf{K}$ and σ in $\mathbf{M}$, $\mathbf{Q}$ are dependent on the function of the density given by (3). Additionally, in (4), $\boldsymbol{V}$ denote the voltage source on each node respectively; l_z is the length in z-direction and set to be 1 m for convenience, ω stands for the angular frequency.

For the case of a single-turn inductor, the elements of $\boldsymbol{V}$ in (4) are known to be $V_{ext}/2$. Combined with the symmetric boundary condition and Dirichlet boundary conditions illustrated in Fig. 1, the value of $\boldsymbol{A}$ can be directly obtained from (4).

For the case of a multi-turn inductor, the algebraic equation (4) is underdetermined and thus requires additional constraints to ensure a unique solution. As illustrated in Fig. 2 (b), the connections between the turns in the multi-turn coil are in series; therefore, the voltage across *Design region n* (n= 1, and 2 in this paper) which keeps unknown, designated as V_n, satisfies with

$$\sum\nolimits_n V_n = V_{ext}/2\,. \tag{8}$$

Meanwhile, according to the current continuity theorem, the total current between each design region is consistent, that is,

$$\int_{\Omega_1} \sigma E d\Omega_1 = \int_{\Omega_2} \sigma E d\Omega_2 = \ldots = \int_{\Omega_n} \sigma E d\Omega_n\,, \tag{9}$$

where Ω_n is the area of *Design region n*, E is the electrical field reading

$$\boldsymbol{E} = -j\omega\boldsymbol{A} + \boldsymbol{V} = -j\omega\boldsymbol{A} + \mathbf{Q}^{-1}\cdot\left(\mathbf{K} + j\omega\mathbf{M}\right)\cdot\boldsymbol{A} \tag{10}$$

in the form of vector after discretization.

Once $\boldsymbol{A}$ and $\boldsymbol{V}$ are obtained through (4), (8) and (9)-(10), the expressions for the magnetic energy W and J_{loss} can be further derived from the electromagnetic field energy theory:

$$W = \frac{1}{4}\boldsymbol{A}^t\cdot\mathbf{K}\cdot\boldsymbol{A}^* = \frac{1}{4}\left(\boldsymbol{A}_r^t\cdot\mathbf{K}\cdot\boldsymbol{A}_r + \boldsymbol{A}_i^t\cdot\mathbf{K}\cdot\boldsymbol{A}_i\right), \tag{11}$$

$$J_{loss} = \frac{1}{2}\boldsymbol{E}^t\cdot\mathbf{M}\cdot\boldsymbol{E}^* = \frac{1}{2}\left(\boldsymbol{E}_r^t\cdot\mathbf{M}\cdot\boldsymbol{E}_r + \boldsymbol{E}_i^t\cdot\mathbf{M}\cdot\boldsymbol{E}_i\right), \tag{12}$$

in which the subscript r and i refer to the real and imaginary parts of corresponding field quantities, respectively.

C. Gradient Computation

To minimize F in (1), L-BFGS-B method [12] is applied for updating the material density distribution from the (p)-th iteration to the $(p+1)$-th iteration, yielding

$$\rho_k^{(p+1)} = \rho_k^{(p)} - \eta^{(p+1)}\mathbf{H}_k\cdot\frac{\partial F}{\partial\boldsymbol{\rho}^{(p)}}\,, \tag{13}$$

where subscript k represents the corresponding value at the node k. In (13), η is the step size, determined through line search, and $\boldsymbol{H}_k$ is the k-th row of the approximate inverse Hessian matrix [12] obtained through gradient information and the material distribution information from the previous iteration. When directly computing the gradient in (13) using (1), the term $\partial\boldsymbol{A}/\partial\rho_k$ arises that is difficult to express in a closed-form solution. To avoid computing it, we adopt the adjoint variable method [13] and construct an approximate expression with using (4):

$$\hat{F} \approx F + \boldsymbol{Z}^t\cdot\left[\left(\mathbf{K} + j\omega\mathbf{M}\right)\boldsymbol{A} - \mathbf{Q}\cdot\boldsymbol{V}\right]. \tag{14}$$

where $\boldsymbol{Z}$ is an auxiliary vector introduced for computational purposes and does not carry any physical meaning. When a sufficiently accurate FEM solution is obtained, F and $\hat{F}$ in (14) become nearly identical, and the value of $\boldsymbol{Z}$ does not affect the approximation between them. Here, we need to use $\boldsymbol{Z}$ to eliminate the computation of $\partial\boldsymbol{A}/\partial\rho_k$, which is defined by the following equation [13]

$$\left(\mathbf{K} + j\omega\mathbf{M}\right)^t\boldsymbol{Z} = \frac{\partial F}{\partial\boldsymbol{A}_r} - \frac{\partial F}{\partial\boldsymbol{A}_i}j\,. \tag{15}$$

By taking the partial derivative of both sides of (14) with respect to ρ_k, eliminating the derivatives of F and $\hat{F}$, applying a transpose operation, and then substituting (15) into the result, we obtain the following approximation:

$$\begin{aligned} 0 \approx\ & \boldsymbol{A}^t\cdot\frac{\partial\left(\mathbf{K} + j\omega\mathbf{M}\right)^t}{\partial\rho_k}\cdot\boldsymbol{Z} \\ & + \frac{\partial F}{\partial\rho_k} + \left[\left(\frac{\partial\boldsymbol{A}_i}{\partial\rho_k}\right)^t\cdot\frac{\partial F}{\partial\boldsymbol{A}_r} - \left(\frac{\partial\boldsymbol{A}_r}{\partial\rho_k}\right)^t\cdot\frac{\partial F}{\partial\boldsymbol{A}_i}\right]j \end{aligned}\,. \tag{16}$$

After rearranging (16) and retaining only the real part, the sensitivity of F can be approximated as

$$\frac{\partial F}{\partial \rho_k} \approx -\mathrm{Re}\left[\boldsymbol{A}^t \cdot \frac{\partial \left(\mathbf{K} + j\omega \mathbf{M}\right)^t}{\partial \rho_k} \cdot \boldsymbol{Z} \right]. \tag{17}$$

Using the relationships among v, σ and ρ, along with the chain rule, (17) can be rewritten as

$$\frac{\partial F}{\partial \rho_k} \approx -\mathrm{Re}\left[\boldsymbol{A}^t \cdot \left(\frac{\partial \mathbf{K}^t}{\partial v_k} \frac{\partial v_k}{\partial \rho_k} \right) \cdot \boldsymbol{Z} + j\omega \boldsymbol{A}^t \cdot \left(\frac{\partial \mathbf{M}^t}{\partial \sigma_k} \frac{\partial \sigma_k}{\partial \rho_k} \right) \cdot \boldsymbol{Z} \right] \tag{18}$$

at the k-th node. Once (15) is solved, $\partial F/\partial \rho_k$ can be obtained via (18) combined with (3).

The terms at the right-hand side of (15) can be expressed as:

$$\frac{\partial F}{\partial \boldsymbol{A}_{r(i)}} = 2\alpha W_1 \frac{\left(L - L_{tar}\right)}{{L_{tar}}^2} \frac{\partial L}{\partial \boldsymbol{A}_{r(i)}} + \alpha W_2 \frac{\partial J_{loss}}{\partial \boldsymbol{A}_{r(i)}}. \tag{19}$$

Now, let us proceed to compute unknown quantities at the right-hand side of (19). From the lumped-parameter circuit energy model, in an inductor under steady-state AC excitation, W and J_{loss} can also be written as

$$W = \frac{1}{4} LI \cdot I^*, \tag{20}$$

$$J_{loss} = \frac{1}{2} RI \cdot I^*, \tag{21}$$

respectively, in which I^*, and R denote the conjugate of I, and the equivalent resistance of the inductor in the right half-plane of the symmetric geometry, respectively. As shown in Fig. 2, in the single-turn case,

$$R = \mathrm{Re}\left[1 \Big/ \left(\frac{1}{R_{1a} + j\omega L_{1a}} + \frac{1}{R_{1b} + j\omega L_{1b}} + \frac{1}{R_{1a} + j\omega L_{1c}} \right) \right], \tag{22}$$

whereas in the two-turn case,

$$R = \mathrm{Re}\left[1 \Big/ \left(\frac{1}{R_{1a} + j\omega L_{1a}} + \frac{1}{R_{1b} + j\omega L_{1b}} + \frac{1}{R_{1a} + j\omega L_{1c}} \right) \right] + \mathrm{Re}\left[1 \Big/ \left(\frac{1}{R_{2a} + j\omega L_{2a}} + \frac{1}{R_{2b} + j\omega L_{2b}} \right) \right] \tag{23}$$

Meanwhile, from Ohm's Law, the relationship between voltage and current in Fig. 2 is given by:

$$V_{ext}/2 = \left(R + j\omega L\right) I. \tag{24}$$

By multiplying both sides of (24) by I^*, we can obtain an expression for the square of the current:

$$I \cdot I^* = \frac{4{J_{loss}}^2 + 16\omega^2 W^2}{\left|V_{ext}/2\right|^2} = 4{J_{loss}}^2 + 16\omega^2 W^2. \tag{25}$$

Then the expression for L and its derivative with respect to $\boldsymbol{A}_{r(i)}$ can be derived to be

$$L = \frac{4W}{I \cdot I^*} = \frac{W}{{J_{loss}}^2 + 4\omega^2 W^2}, \tag{26}$$

$$\frac{\partial L}{\partial \boldsymbol{A}_{r(i)}} = 4 \frac{\left(I \cdot I^*\right) \dfrac{\partial W}{\partial \boldsymbol{A}_{r(i)}} - W \dfrac{\partial \left(I \cdot I^*\right)}{\partial \boldsymbol{A}_{r(i)}}}{\left(I \cdot I^*\right)^2}. \tag{27}$$

When using (20) and (25), (27) also equals

$$\frac{\partial L}{\partial \boldsymbol{A}_{r(i)}} = \frac{\left({J_{loss}}^2 + 4\omega^2 W^2\right) \dfrac{\partial W}{\partial \boldsymbol{A}_{r(i)}}}{\left({J_{loss}}^2 + 4\omega^2 W^2\right)^2} - \frac{W\left(2J_{loss} \dfrac{\partial J_{loss}}{\partial \boldsymbol{A}_{r(i)}} + 8\omega^2 W \dfrac{\partial W}{\partial \boldsymbol{A}_{r(i)}} \right)}{\left({J_{loss}}^2 + 4\omega^2 W^2\right)^2} \tag{28}$$

Then combining (19), (26) and (28), it can be concluded that the derivatives of F with respect to $\boldsymbol{A}_{r(i)}$ can be expressed in terms of W, J_{loss} and their derivatives with respect to $\boldsymbol{A}_{r(i)}$. By differentiating (11) and (12) with respect to $\boldsymbol{A}_{r(i)}$, we can obtain

$$\frac{\partial W}{\partial \boldsymbol{A}_{r(i)}} = \frac{1}{4}\left(\mathbf{K} + \mathbf{K}^t\right) \cdot \boldsymbol{A}_{r(i)}, \tag{29}$$

$$\frac{\partial J_{loss}}{\partial \boldsymbol{A}_{r(i)}} = \frac{1}{2}\left(\mathbf{M} + \mathbf{M}^t\right) \cdot \boldsymbol{E}_{i(r)}^t \circ \frac{\partial \boldsymbol{E}_{i(r)}^t}{\partial \boldsymbol{A}_{r(i)}}. \tag{30}$$

Subsequently, by substituting (29)-(30) into (26)-(27), and then incorporating the resulting expressions together with (30) into (19), we can ultimately derive the right-hand side of (15), from which $\boldsymbol{Z}$ can be computed. Finally, by substituting the computed $\boldsymbol{Z}$ into (18), the derivative of F with respect to the density is finally obtained.

Based on the aforementioned method, the nodal material density is updated iteratively using (13). The optimization procedure continues until the change in F between two consecutive iterations becomes smaller than a predefined convergence tolerance, at which point the process is considered to have converged and is terminated.

III. Optimization Results

The coefficients W_1 and W_2 in (1) are taken equal to 0.60 and 0.50 respectively, and α=100. In this study, the length of each design region l=1 mm. The skin depth is equal to 0.3 mm for the copper at 50 kHz, one thirds of the design region. The eddy current effect cannot be negligible. For the inductor with single-turn coil, ΔL= 0.0 mm, and for the one with two-turn c α oil, ΔL= 1.0 mm.

A. Case Study of a Single-Turn Coil

In this case, a 2D inductor with L_{tar}=8.0 μH with minimized Joule loss is designed by the proposed method. The initial topology in *Design region* 1 is configured with four uniformly distributed cylinders, each with a radius of 0.2 mm. A material with ρ= 0.7 is assigned inside the cylinders, while the surrounding region is filled with a material of ρ= 0.3, as shown in Fig. 4 (a). The inductance and Joule loss under the initial topology are 4.91 μH and 0.086 W, respectively.

After 69 iterations, the optimal design that meets the specified requirements is successfully obtained, shown in Fig. 4. Additionally, design solutions the 5th and the 15th iteration are also presented for comparison. It is observed that the topology gradually converges toward the center, forming a star-like pattern.

To verify that the optimized topology achieves performance closer to the design target, the details of the convergency history are also given in Fig. 5. It can be observed that F stabilizes finally. Meanwhile, the inductance gradually approaches the target design value (L= 7.85 μH at the 69th

iteration) with the minimum error being only 1.9%, and the Joule loss decreases progressively until it stabilizes (J_{loss}= 0.014 W at the 69th iteration).

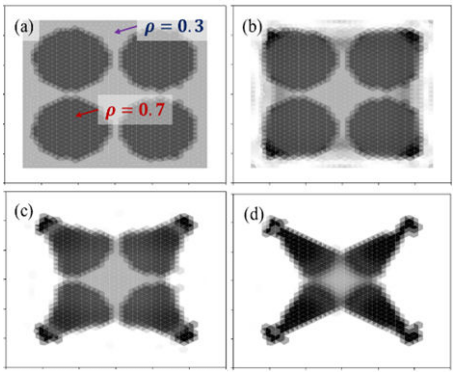

Fig. 4. The grayscale representation of design solutions, where black corresponds to copper and white represents iron. (a) Initial shape. (b) Design at the 5th iteration. (c) Design after the 15th iteration. (d) Final optimal solution.

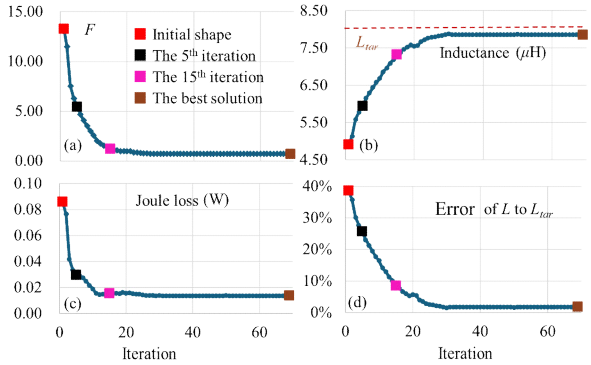

Fig. 5. Convergence history. (a) Convergency history for F. (b) Inductance convergence curve. (c) Evolution of J_{loss} over iterations. (d) Errors of L with respect to L_{tar} over iterations.

Despite the optimal solution is obtained in Fig. 5, the solution, so called composite solution, is based on a continuous variation of the density ρ. Therefore, to obtain a solution made with iron and copper, it is necessary to reclassify the materials to obtain the final, physically realizable topology. Specifically, elements with $\rho < 0.5$ are categorized as iron, while those with $\rho \geq 0.5$ are categorized as copper. After the classification of materials, finally the topology structure is illustrated Fig. 6 (a). The inductance value is 7.86 μH, and the Joule loss is 0.013 W, which are very close to the optimal fictitious composite solution. Furthermore, the contour of $\boldsymbol{A}$, as well as the distribution of current density for both the real and the imaginary component, are is presented in Fig. 6 to illustrate its electromagnetic behavior.

B. Case Study of a Two-Turn Coil

In this case, a two-turn inductor of L_{tar}=30.0 μH with minimized Joule loss is designed. The initial topology in *Design region* 1 and *Design region* 2 is configured with four uniformly distributed cylinders of a radius being 0.2 mm and 0.25 mm respectively, as shown in Fig. 7 (a). The material with ρ= 0.7 is assigned inside the cylinders, while the surrounding region is filled with a material of ρ= 0.3. The inductance and Joule loss under the initial topology are 13.3 μH and 0.023 W, respectively.

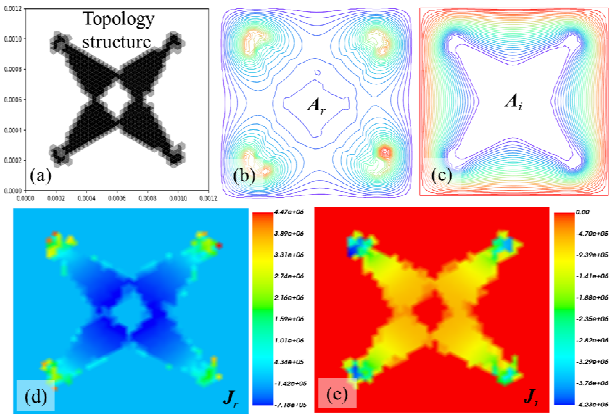

Fig. 6. Optimized structure and the field distribution. (a) Topology after the category. (b) Contour of $\boldsymbol{A}$ for the real part. (c) Contour of $\boldsymbol{A}$ for the imaginary part. (d) Current density for the real part ($\boldsymbol{J}_r$). (e) Current density for the imaginary part ($\boldsymbol{J}_i$).

After 72 iterations, the optimal design that meets the specified requirements is successfully obtained, shown in Fig. 7 (d). Additionally, design solutions the 5th and the 15th iteration are also presented for comparison. After the optimization, it can be observed that the lengths and widths of the coils in *Design Regions* 1 and *Design region* 2 become comparable, which is a clear departure from their initial configurations.

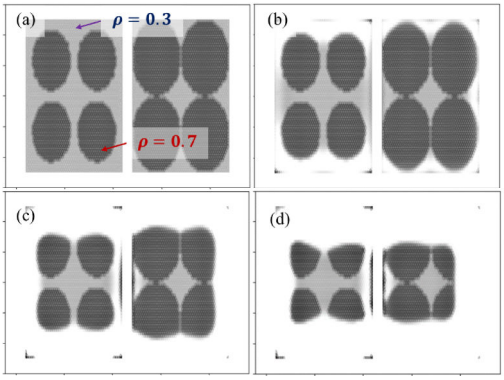

Fig. 7. The grayscale representation of design solutions. (a) Initial shape. (b) Design at the 5th iteration. (c) Design after the 15th iteration. (d) Final optimal solution.

Similarly, the convergence information is also provided, as shown in Fig. 8. It is evident that starting from iteration 25, the convergence gradually becomes more stable until stop. The final optimized topology at the 72nd iteration yields an inductance of 30.4 μH and a Joule loss of 0.012 W. The inductance deviates from the target value by only 1.2%. After classifying the continuously varying material distribution, we obtain the final physical topology, as shown in Fig. 9. Eventually, the inductance and Joule loss of Fig. 9 are 30.08 μH and 0.011 W, respectively, which are very close to the final results of the fictitious composite solution from the optimization.

In addition, we present the contours of $\boldsymbol{A}$ and the current density of the final structure, as shown in Fig. 10 and Fig. 11, respectively.

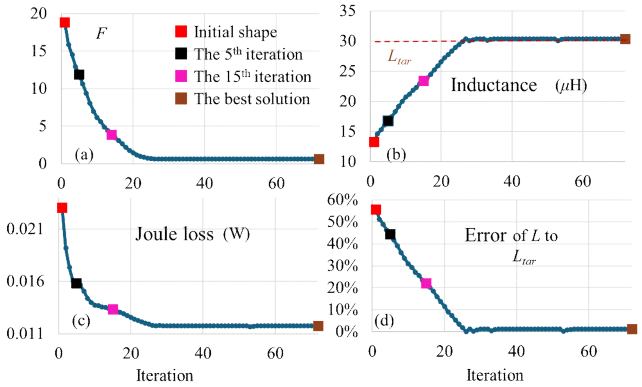

Fig. 8. Convergence history. (a) Convergency history for F. (b) Inductance convergence curve. (c) Evolution of J_{loss} over iterations. (d) Errors of L with respect to L_{tar} over iterations.

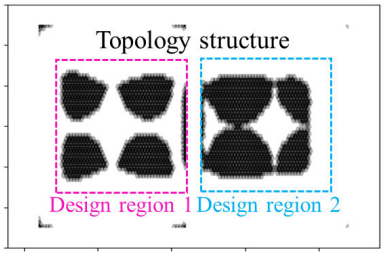

Fig. 9. Optimized structure after the category.

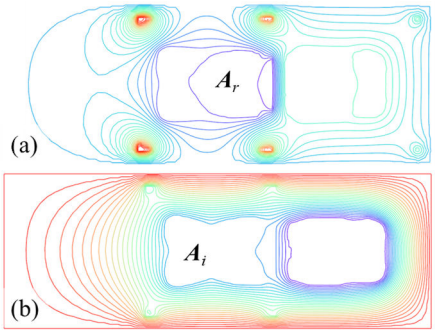

Fig. 10. Contour of $\boldsymbol{A}$. (a) Real part. (b) Imaginary part.

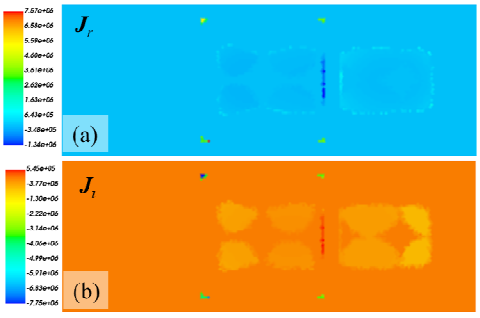

Fig. 11. Current density. (a) Real part. (b) Imaginary part.

IV. Conclusion

In this paper, a novel optimization framework for chip inductors has been developed, targeting both the satisfaction of specified inductance values and the minimization of eddy current losses. With the usage of field-circuit coupling method, it enables the analysis of inductors under complex coil configurations involving both series and parallel connections. The results on both single-turn and two-turn inductors validate the effectiveness and generality of the proposed method. However, it is observed that the current topology results exhibit some roughness due to mesh dependency. Future work will focus on incorporating density filtering techniques to improve the smoothness of the optimized structures, and the optimization results under strong skin-effect conditions.

Acknowledgment

This work is supported by the National Natural Science Foundation of China under Grant 52507019.

References

[1] Ziyang Wang, Wucheng Ying, Yinong Zeng, et al., “Equally Split PCB Inductor (ESPI) Design for High Energy Density and Low Near-Field Radiation”, *IEEE Transactions on Power Electronics*, vol. 39, no. 5, pp. 4963-4968, May 2024.

[2] A. Namadmalan, “Modeling of High Power Inductors Based on Solid Flat Wires for Compact DC-DC Converters, ”*2024 IEEE Kansas Power and Energy Conference (KPEC)*, Manhattan, KS, USA, 2024, pp. 1-5.

[3] Shen Wang, M. A. de Rooij, W. G. Odendaal, et al, “Reduction of High-frequency Conduction Losses Using a Planar Litz Structure,” *IEEE 34th Annual Conference on Power Electronics Specialist*, Acapulco, Mexico, 2003.

[4] Ignacio Lope, Claudio Carretero, Jesus Acero, et al., “Frequency-Dependent Resistance of Planar Coils in Printed Circuit Board with Litz Structure,” *IEEE Transactions on Magnetics*, vol. 50, no. 12, pp. 1-9, Dec. 2014, Art no. 8402409.

[5] Reda El Bechari, Vincent Martin, Frédéric Gillon, et al., “From Topology Optimization to 3-D Printing of an Electromagnetic Core,” *IEEE Transactions on Magnetics*, vol. 59, no. 5, pp. 1-4, May 2023, Art no. 9200704.

[6] Feng Guo, Ian P. Brown, “Simultaneous Magnetic and Structural Topology Optimization of Synchronous Reluctance Machine Rotors,” *IEEE Transactions on Magnetics*, vol. 56, no. 10, pp. 1-12, Oct. 2020, Art no. 8101612.

[7] Adrien Thabuis, Xiaotao Ren, Guillaume Burnand, et al., “Density-Based Topology Optimization of Conductor Paths for Windings in Slotted Electrical Machines,” *2019 22nd International Conference on Electrical Machines and Systems (ICEMS)*, Harbin, China, 2019, pp. 1-6.

[8] Adrien Thabuis, Xiaotao Ren, Yves Perriard, “Topology Optimization of Motor Windings for Coreless Electrical Machines,” *2024 IEEE Energy Conversion Congress and Exposition (ECCE)*, Phoenix, AZ, USA, 2024, pp. 5802-5809.

[9] Shuli Yin, Hajime Igarashi, “Integrated design of inductors using Monte Carlo tree search based on three-dimensional model,” *International Journal of Applied Electromagnetics and Mechanics*. vol. 78, no. (1-3), pp. 269-274.

[10] Hajime Igarashi, *Topology Optimization and AI-based Design of Power Electronic and Electrical Devices*, London: Academic Press, 2024.

[11] S. J. Salon, *Finite Element Analysis of Electrical Machines*. Boston: Kluwer academic publishers, 1995.

[12] Ciyou Zhu, Richard H. Byrd, Peihuang Lu, et al, “Algorithm 778: L-BFGS-B: Fortran subroutines for large-scale bound-constrained optimization”, *ACM Transactions on mathematical software (TOMS)*, vol. 23, no. 4, pp. 550-560, 1997.

[13] Hajime Igarashi, and Kota Watanabe, “Complex Adjoint Variable Method for Finite-Element Analysis of Eddy Current Problems,” *IEEE Transactions on Magnetic*, vol. 46, no. 8, pp. 2739- 2742, 2010.